Nanoscale Advances

ROYAL SOCIETY OF CHEMISTRY

PAPER

View Article Online
View Journal | View Issue

Cite this: *Nanoscale Adv.*, 2025, **7**, 6475

Amyloid formation of mutated Alzheimer's Aβ 16–36 residues peptide and application in toxic lead and uranium ion binding

Aishwarya Natarajan, [ab] Late Ramakrishna Vadrevu,[b] Aruna Jyothi Kora [cd] and Krishnan Rangan *[a]

Amyloid nanostructures are gaining attention as bio-compatible materials with diverse potential applications. The formation/self-assembly of amyloid fibrils, though implicated in the prognosis of several neurodegenerative diseases, contrastingly can also be explored for their functional properties owing to their unique stability and strength. The physicochemical environment and amino-acid composition are characteristic and specifically crucial for a protein/peptide to form amyloid fibrils. The Aβ peptide involved in the Alzheimer's disease prognosis consists of two central hydrophobic core regions and a central polar region forming a β-hairpin. In this study, a 21 amino acid containing peptide KLVFFAEDVESNRGAIIGLMV is designed introducing point mutations to the original 16–36 residues of the Aβ peptide (G → E at position 25 and K → R at position 28), resulting in a modified Aβ peptide variant. The self-assembling nature of this modified peptide has been explored, and ThT fluorescence and circular dichroism spectroscopy exhibit β-sheet structures. Detailed morphological analysis using SEM, AFM, and confocal microscopy revealed a progression from initial blob-like spongy forms to protofibrils, culminating in branched amyloid fibrils. These strategic mutations enable binding of toxic metals such as uranium and lead, as demonstrated *via* UV-visible spectroscopy, XPS, AAS and fluorescence spectroscopy, highlighting its promise for environmental remediation.

Received 7th March 2025
Accepted 5th August 2025

DOI: 10.1039/d5na00228a

rsc.li/nanoscale-advances

1 Introduction

Research on the self-assembly of supramolecular amyloid fibrils highlights its potential for applications like water purification and removal of toxic heavy metals, with studies pointing to amyloid–carbon membranes and amyloid coacervation techniques as promising methods.[1–5] The formation of natural biomaterials like silks and glues involves protein–metal interactions, critical for designing biomaterials with specific metal binding properties, drawing insights from nature and evolution.[6–8] This concept supports exploring metal ion binding in engineered peptide-based materials as an alternative to traditional physicochemical approaches for sustainable remediation.[9] Metal ions are also implicated in neurodegenerative diseases like Alzheimer's by binding amyloid peptides and contributing to plaque formation. These interactions—especially with Cu, Zn, and Fe—promote aggregation and misfolding, influencing disease progression. Specific residues such as glutamic acid, aspartic acid, and histidine are critical for metal ion coordination in the amyloid β peptide.[10–12]

Amyloid beta (Aβ 1–42/Aβ 1–40) peptide is known for amyloid formation and metal binding through amino acid side chains, and could offer a method for creating mutations at the amino acid level to improve heavy metal binding. Developing new self-assembling peptides could enhance purification processes by increasing surface area and binding specificity by arranging amino acid residues. Building on this natural metal-binding propensity, we aimed to develop a self-assembling peptide-amyloid material capable of binding to toxic metals by modifying the Alzheimer's amyloid β peptide, specifically the 16–36 residues (KLVFFAEDVGSNKGAIIGLMV), which consist of two amyloid forming regions, and a turn region known as the central polar region. By altering the sequence to KLVFFAED-VESNRGAIIGLMV, and substituting G → E at position 25 and K → R at position 28, we maintained the hydrophobic core while introducing mutations that allow metal-binding. This design leverages the structure of amyloids to potentially capture toxic metals effectively. The resulting 21 residue modified amyloid β (*mAβ21*) peptide developed, designed to include metal-binding residues like aspartic acid, glutamic acid, and arginine, forms amyloid-like nanofiber structures. Their structural

[a]*Department of Chemistry, Birla Institute of Technology and Science Pilani, Hyderabad Campus, Jawahar Nagar, Hyderabad 500 078, Telangana, India. E-mail: rkrishnan@hyderabad.bits-pilani.ac.in*

[b]*Department of Biological Sciences, Birla Institute of Technology and Science Pilani, Hyderabad Campus, Jawahar Nagar, Hyderabad 500 078, Telangana, India*

[c]*National Centre for Compositional Characterisation of Materials (NCCCM), Bhabha Atomic Research Centre, ECIL PO, Hyderabad 500 062, India*

[d]*Homi Bhabha National Institute (HBNI), Anushakti Nagar, Mumbai-400 094, India*

properties were explored through ThT fluorescence, circular dichroism, SEM, and AFM techniques. The peptide's effectiveness in binding lead and uranyl ions was specifically investigated using spectroscopic methods like UV-vis absorption, fluorescence, atomic absorption, and X-ray photoelectron spectroscopy.

2 Materials and methods

All chemicals were obtained from Sigma Aldrich/Merck. The lyophilized powder of peptide Ac-KLVFFAEDVESNRGAIIGLMV-$CONH_2$ (*mAβ21*) was obtained from Shanghai A peptide. To avoid charges at the amine and carboxy terminals, the N- and C-termini were acetylated and amidated, respectively. HPLC and mass spectrometry were used to confirm the purity and molecular weight of the custom-synthesized peptide, as shown in Fig. S1 and S2.

2.1 Peptide sample preparation

In order to remove any pre-formed aggregates, 0.5 mg of the lyophilized *mAβ21* peptide was weighed and dissolved in 500 μL of 1,1,1,3,3,3-hexafluoro-2-propanol (HFIP) and then placed overnight in a fume hood for evaporation of HFIP. Subsequently, the residual HFIP was entirely evaporated using a vacuum in the Concentrator Plus (Eppendorf), resulting in a thin film of peptide in the vial. *mAβ21* peptide was then dissolved in 1 mL aqueous buffer at pH 12.0 with pH adjustments made using HCl and NaOH. A NanoDrop One spectrophotometer (Thermo Scientific) was employed to ascertain peptide concentrations, resulting in a measurement of approximately 0.5 mg mL^{-1}, obtained by measuring the absorption of the peptide at 205 nm with a molar extinction coefficient of 31 mg^{-1} cm^{-1}.[13]

2.2 Thioflavin T fluorescence assay

ThT dye, when bound to β-sheet structures, results in a significant increase in fluorescence intensity and, therefore, was used to measure the formation of amyloid-like structures by tracking the kinetics of the amyloidation reaction. 3 mg of ThT dye was dissolved in 10 mL of MilliQ water and filtered with a 0.2 μm syringe filter to obtain the stock ThT solution. The concentration was determined by measuring the absorbance at 416 nm on a Jasco V650 UV-visible spectrophotometer after diluting the stock solution and using a molar extinction co-efficient of 26 620 M^{-1} cm^{-1} (ref. 14 and 15) 10 μM of ThT dye solution was added to around 20 μM of *mAβ21* peptide solution, and the fluorescence intensity changes were measured at different time intervals. Fluorescence spectra were obtained using a Jasco FP-6300 spectrofluorometer, with the emission spectra recorded in the range of 450 to 550 nm and the excitation wavelength set at 440 nm. Each spectrum represents an average of three acquisitions and has been buffer-corrected.

2.3 Circular dichroism spectroscopy

The far-UV CD spectra of the *mAβ21* peptide solution (100 μM) were measured using a Jasco J1500 CD spectrometer. CD spectra were collected in the range of 195–250 nm utilizing a 2 mm path length cuvette at 25 °C. For each sample, an average of three measurements was recorded at a scanning speed of 100 nm min^{-1}, a data integration period of 4 seconds, and a bandwidth of 2.5 nm.[16]

2.4 Dynamic light scattering

The particle size of the synthesized amyloid peptide was assessed using a Nano-ZS Zetasizer (Malvern Instruments Ltd, UK). 100 μM concentration of the peptide (*mAβ21*) was recorded at room temperature in a single-use cuvette with a path length of 1 cm. Three scans were run for each sample, each consisting of 16 runs.

2.5 Scanning electron microscopy

Field Emission Scanning Electron Microscopy (FE-SEM) was employed to investigate the formation and morphology of the self-assembled structures. To minimize salt crystallization artifacts, the peptide samples were washed thoroughly (3 times) with ultrapure Milli-Q deionized water prior to drying, in order to remove residual buffer salts. Then, 5 μL of the washed *mAβ21* peptide sample was carefully placed on a glass coverslip and air-dried at room temperature for 30 minutes under dust-free conditions. The dried coverslip was then securely mounted on a brass stub using carbon tape. The samples were coated with a 6 nm gold layer using a Leica Ultra Microtome EM UC7 Sputter Coater at a current setting of 20 mA for 1 minute. SEM imaging was carried out at an accelerating voltage of 20 kV using an Apreo LoVac (FEI, Thermo Scientific).

2.6 Atomic force microscopy

To prepare samples for atomic force microscopy (AFM), we followed a method similar to that used for scanning electron microscopy. 5 μL of the peptide sample was drop-cast on a glass coverslip and air dried for 30 minutes. We obtained AFM images using a SPM Solver Nano system and a NT-MDT image processor. The atomic force microscope was operated in tapping mode at room temperature, with the scan window size set between 20 cm^2 and 90 cm^2 and a scan rate of 0.8 Hz.

2.7 Confocal microscopy

Fluorescence and bright-field images of the samples were obtained using a confocal microscope (TCS-SP8; Leica, Wetzlar, Germany). For imaging, 5 μL of the sample was drop-cast onto a glass coverslip and inverted onto a glass slide. Spectral analysis was performed using a 405 nm laser for excitation, with a 20 nm emission bandwidth. Observations were conducted under a 20× objective. No external fluorescent dye was used; the detected fluorescence arises from the intrinsic emission of the peptide, which exhibited a characteristic emission peak at ~450 nm under 355 nm excitation.

2.8 Zeta potential measurements and pH potentiometric titration

A Nano-ZS Zetasizer was used to perform zeta potential (mV) studies for the peptide solutions at pH levels ranging from 2 to

12, which were prepared by the addition of HCl (1 M) and NaOH (1 M). Potentiometric titrations were carried out to measure the pH of the peptide solutions against 1 M NaOH and monitored with a glass microelectrode connected to an Eutech Instruments pH meter.

2.9 UV absorption spectroscopy for lead binding

UV-visible absorption spectra of lead(II) acetate solution, self-assembled *mAβ21* (pH 12) peptide solution and the peptide amyloid–lead solution were recorded on a Jasco V650 Spectrophotometer in the wavelength range of 190–600 nm at room temperature, using a 1 cm path length cuvette and bandwidth of 1 nm. We carefully monitored the UV spectra at various lead concentrations (15, 30, 45, 60, 75, and 90 μM or 5, 10, 15, 20, 25, and 30 ppm) while consistently maintaining the peptide concentration as 50 μM throughout the experiments.

2.10 Atomic absorption spectroscopy

10 μM of self-assembled *mAβ21* peptide solutions were incubated with the 15 μM lead acetate metal solution for 12 h at room temperature. The peptide–metal complex solutions were filtered, and the filtrates were analyzed for metal ion content using an AA-7000 Atomic Absorption Spectrophotometer (Shimadzu). A standard curve was generated using lead acetate solutions of known concentrations, which enabled the determination of unknown concentrations in the peptide–metal solutions following incubation. For the specificity of the selected metal binding study, 50 μM of peptide amyloid in 10 mL solution containing 5 ppm of each metal ion (Pb^{2+}, Cr^{3+}, Co^{2+}, Ni^{2+}, Hg^{2+}, Zn^{2+}, Cu^{2+}, and Ca^{2+}) were incubated overnight and filtered through a 5 kDa cut-off membrane filter. The filtrate solution was again analysed using an atomic absorption spectrophotometer.

2.11 X-ray photoelectron spectroscopy

X-ray photoelectron spectroscopy (XPS) studies were conducted on peptide and metal-bound forms using a Thermo Scientific K-Alpha instrument equipped with an Al Kα X-ray micro-focused monochromator source. This analysis was performed under a vacuum pressure of 1.5×10^{-7} mbar, and carbon corrections were applied utilizing Avantage software. Sample preparation involved incubating a 300 μL solution containing 50 μM of peptide and 45 μM of lead acetate overnight at pH 12. For studies focused on uranium binding, a separate 300 μL solution containing 60 μM of peptide at pH 12 was incubated overnight with 25 μM of uranyl nitrate. Subsequently, 5 μL of each peptide–metal complex solution was applied to 5 mm × 5 mm glass slides, which were dried to create thin films before being transferred to the XPS sample holder. XPS survey scan spectra for each sample were recorded across a binding energy range of 0–1300 eV, with each spectrum representing an average of five scans. High-resolution narrow-band spectra for Pb 4f, U 4f, N 1s, O 1s, and C 1s were obtained, averaging ten scans to facilitate quantitative binding energy measurements. The spectral analysis was conducted using Fityk software, ensuring accurate interpretation of the binding energy data.[17]

2.12 Arsenazo-III assay for uranium binding

Uranyl stock solution was made by dissolving 1 mg of uranyl nitrate in 1 mL of water to obtain a 1000 ppm (2.53 mM) solution, which was then diluted to create a stock solution of 100 ppm (0.253 mM). A 0.1% (1.29 mM) arsenazo III (3,6-bis((*E*)-(2-arsonophenyl)diazenyl)-4,5-dihydroxynaphthalene-2,7-disulphonic acid) was prepared in water. For subsequent absorbance measurements, 20 μL of the 1.29 mM arsenazo III reagent was added to a 5 ppm uranyl nitrate solution, and the final volume was brought to 2 mL. The resulting mixture was allowed to equilibrate for 5 minutes prior to spectral analysis carried out in the visible range from 350 nm to 900 nm. For investigating peptide amyloid–uranium binding interactions, the uranyl arsenazo complex was mixed with various concentrations of amyloid peptides. A solution containing 5 ppm uranyl nitrate (12.9 μM) was combined with 12.9 μM of arsenazo III dye in a 1 : 1 ratio and incubated overnight with peptide concentrations of 20, 40, 60, and 80 μM. After incubation, the amyloid–uranium solution was filtered through a 3 kDa cut-off filter and centrifuged at 5000 rpm for 20 minutes. The absorption spectra of the filtrates were recorded to assess the extent of reduction in the concentration of the uranyl-arsenazo complex attributed to the binding interactions with the amyloid peptides.

2.13 Fluorescence quenching study for uranium binding

Fluorescence quenching of uranyl nitrate by peptide amyloids was performed using a microplate reader (SpectraMax iD3, Molecular Devices, with SpectraMax software) using λ_{ex} = 266 nm and λ_{em} = 522 nm. Various concentrations of the self-assembled peptide amyloids, ranging from 5 to 70 μM, were added to wells containing a 10 ppm (25 μM) uranyl nitrate solution. The excitation wavelength was set to 266 nm, and fluorescence spectra were recorded within 450 nm to 650 nm. All measurements were conducted in triplicate to ensure data accuracy and reliability.

The fluorescence quenching process was examined for both static and dynamic quenching mechanisms, given the expected formation of a metal–peptide complex upon the initial addition of the peptide. The Stern–Volmer quenching constant (K_{SV}) was derived from the linear portion of the plot of $[F_0/F]$ against [Q] at lower peptide concentrations, following the Stern–Volmer equation.[18]

$$\frac{F_0}{F} = 1 + K_{SV}[Q]$$

In this context, F_0 and F denote the fluorescence intensity of the uranyl nitrate solution in the absence and presence of the peptide, respectively, while [Q] represents the concentration of the peptide. The binding constant (K_A) for the interaction between uranium and the peptide was acquired from the linear plot of $[(F_0 - F_m)/(F_0 - F)]$ *vs.* 1/[Q], where F_m corresponds to the fluorescence intensity measured at saturating peptide

concentrations, consistent with the 1 : 1 binding profile outlined by the Benesi–Hildebrand equation.[19]

$$\frac{1}{[F_0 - F]} = \frac{1}{[F_0 - F_m]} + \frac{1}{K_A[Q][F_0 - F_m]}$$

3 Results and discussion

3.1 Peptide design and optimization

In the native sequence of the Alzheimer's amyloid β (Aβ) peptide, the 16–36 residues consist of KLVFFAEDVGSNKGAIIGLMV residues (Fig. 1 (A)), where KLVFFA (16–21 residues) and GAIIGLMV (29–36 residues) correspond to the β-sheet steric zipper forming hydrophobic core region, and the β-turn/β-hairpin forming the EDVGSNK (22–28) region is an important structural motif in the Aβ aggregation pathway. The Aβ 1–42 peptide with PDB ID 5OQV was analyzed using PyMOL after removing residues 1–15 and 37–42, focusing on residues 16–36. Mutations G → E at position 25 and K → R at position 28 were introduced, as shown in Fig. 1(B) and (C). The mutated structure, post energy minimization *via* Swiss-PDB viewer, had an energy of −91.822 kJ mol^{-1}, compared to −14.947 kJ mol^{-1} for the original segment.[12]

The mutation of G → E at position 25 serves to provide the glutamic acid (carboxylic acid side chain) residue, which is known to be the highest contributor (38%) as a ligand for Pb(II) complexation in protein crystal structures and the additional mutation K → R provides a preference for uranyl ion binding through hydrogen bonding interactions.[20] Glutamic acid (E25) and aspartic acid (D23) residues that can bind effectively to lead metal ions are depicted in Fig. 2(A), where the closest distances between these residues (E25 and D23) of two adjacent strands in the amyloid-forming mutated KLVFFAEDVESNRGAIIGLMV (*mAβ21*) are seen. Similarly, the closest distance between arginine (R28), glutamic acid (E25), and aspartic acid (D23) is shown in Fig. 2(B), which can also potentially form a pocket known to bind to the axial oxygen of a uranyl ion.[20] The structures/models obtained were created by using the mutated version of the 5OQV PDB file consisting of the modified sequence KLVFFAEDVESNRGAIIGLMV (*mAβ21*) and retaining only residues E25 and D23 as shown in Fig. 2(A), and R28, E25, and D23 as shown in Fig. 2(B). The distances between the adjacent residues were calculated by the measurement wizard present in the PyMOL software, and a suggestive image of the binding pockets assumed by two adjacent amyloid strands was generated.[12]

The designed twenty-one amino acid residue containing peptide KLVFFAEDVESNRGAIIGLMV (*mAβ21*), acetylated at the N terminal and amidated for end group protection at the C terminal, was obtained and purified on an HPLC system using 0.1% trifluoroacetic acid (TFA) in water and acetonitrile as solvent systems by the gradient elution method (Fig. S1). For clear visualisation of functional groups, a molecular structural scheme of the peptide Ac-KLVFFAEDVESNRGAIIGLMV-$CONH_2$ is depicted in Scheme 1. The ESI(+)-MS data confirmed the designed peptide structure, which showed mass peaks at *m*/*z* values of 1176.35 and 784.50, which are correspondingly assigned for di-protonated $[M + 2H]^{2+}$ and tri-protonated $[M + 3H]^{3+}$ molecular ion peaks respectively, as shown in Fig. S2. The predicted monoisotopic mass of neutral *mAβ21* peptide $C_{107}H_{173}N_{27}O_{30}S$ is 2348.256.

3.2 Structural characterization of Aβ 1–42 based designed *mAβ21* peptide amyloid formation

3.2.1 ThT fluorescence spectroscopy. Thioflavin T (ThT) based fluorescence and circular dichroism (CD) spectra were recorded for assessing the amyloid-forming nature and

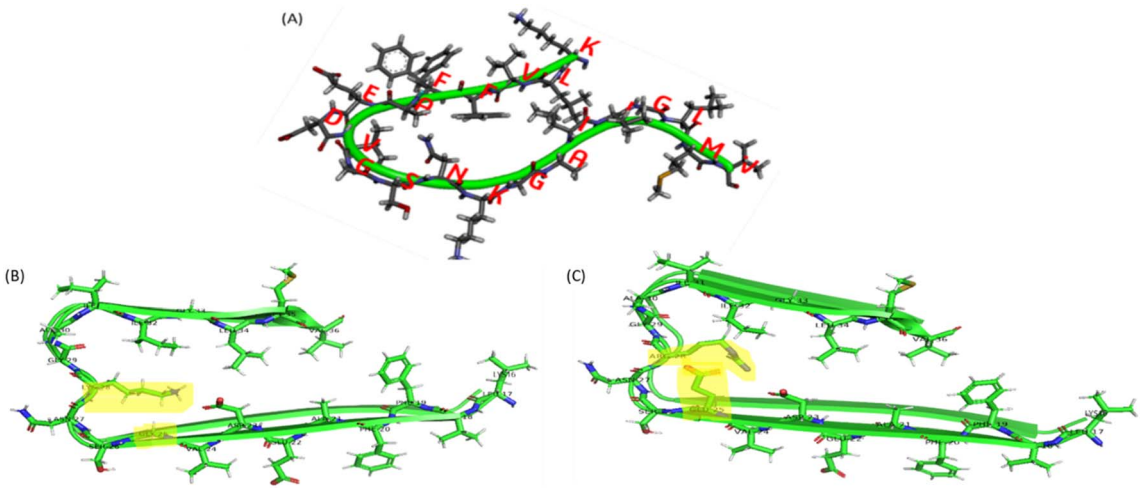

Fig. 1 (A) KLVFFAEDVGSNKGAIIGLMV 16–36 amino acid residue part of the native Aβ 1–42 peptide, PDB ID-5OQV and (B) the original sequence of 16–36 residues (KLVFFAEDVGSNKGAIIGLMV) of the native Aβ peptide, with the G25 and K28 residues highlighted. (C) Modified sequence (KLVFFAEDVESNRGAIIGLMV) of 16–36 residues of Alzheimer's Aβ peptide. The original 16–36 residue Aβ peptide has been modified with two mutations, G → E at position 25 and K → R at position 28. The images were created by downloading the PDB structure (5OQV) and visualizing and mutating the structure on PyMOL, followed by energy minimization on SPDBV.

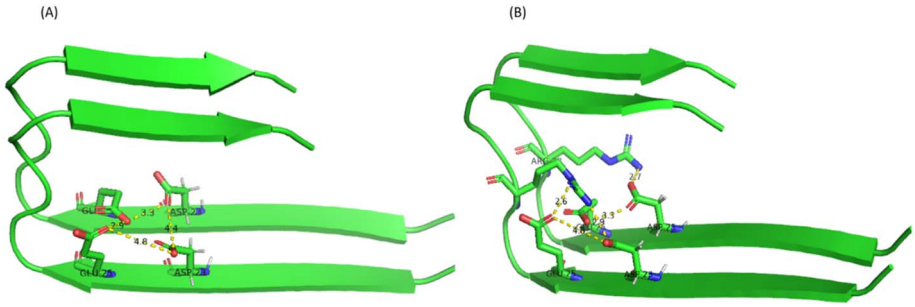

Fig. 2 Suggestive structure/model depicting the closest distance between (A) amino acids E25 and D23 forming a binding pocket that has the affinity to bind to the lead metal ion, and (B) RED (R28, E25, and D23) forming a binding pocket that has an affinity to bind to axial oxygen atoms of a uranyl ion.

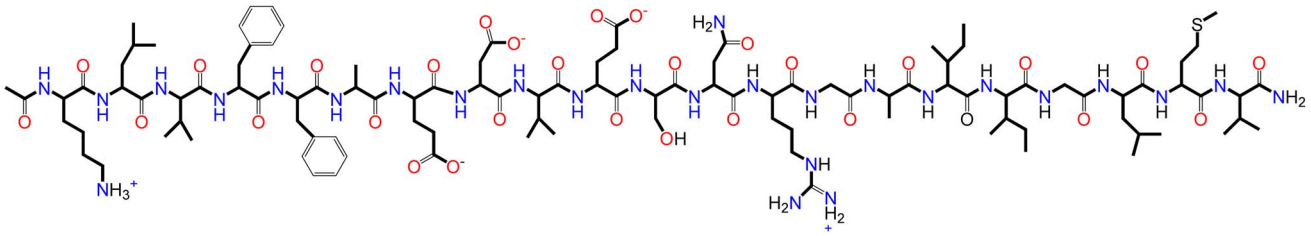

Scheme 1 Chemical structure of the designed Ac-KLVFFA**ED**V**ES**N**R**GAIIGLMV-CONH$_2$ peptide at neutral pH. Potential metal binding sites are shown in bold letters.

structure adopted by the *mAβ21* peptide at an alkaline pH of 12.0. The alkaline pH was selected for amyloid formation owing to a previous report of acetylated KLVFF forming fibrils at pH 12.[21] The peptide was investigated for its ability to self-assemble into higher-order fibrils by following the kinetics of formation through a change in the fluorescence intensity of the amyloid-specific dye, thioflavin T (ThT). A typical ThT assay for tracing the nucleation-dependent peptide amyloid forming polymerization process shows a sigmoidal trend that is characteristic of a lag phase (monomers that are oligomerizing), protofibrils which are detected in the log phase (growth phase) where the thioflavin T molecule binds to the maturing β-sheets of the fibrils and finally, a stationary phase of mature fibrils that is saturated. In the absence of peptide, thioflavin T shows fluorescence emission at around 450 nm under 350 nm excitation.[14,15] The concentration of the ThT stock solution prepared was 9.4×10^{-4} M. A solution combination was generated by combining 10 μL (9.4×10^{-4} M) of ThT solution and 100 μL (2.1×10^{-4} M) of peptide solution, resulting in a total volume of 1 mL. The fluorescence spectra were recorded at various time intervals for a peptide solution containing 21 μM *mAβ21* peptide, which was introduced to a ThT solution at a concentration of 10 μM. Upon binding to amyloid fibrils, ThT gives a strong fluorescence signal at approximately 490 nm when excited at 440 nm. After dissolution in an aqueous buffer at pH 12, the peptides were incubated with the dye at a ratio of 2 : 1 (peptide amyloid : ThT). A fluorescence intensity enhancement was studied with the peptide amyloid formation process in the presence of thioflavin T (Fig. S3 and Table S1). A relative fluorescence intensity enhancement of ThT + *mAβ21* peptide recorded at 490 nm *vs.* time is depicted in Fig. 3, indicating the trend followed by the self-assembled peptide structure. A sigmoidal fluorescence intensity transition was observed from the beginning of the incubation of the peptides to about 80–100 hours. The ThT–peptide amyloid fluorescence study infers that

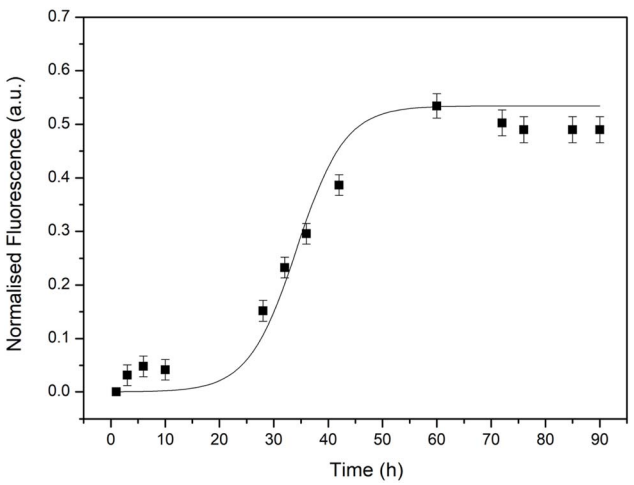

Fig. 3 Thioflavin T (ThT) fluorescence enhancement assay showing the time-dependent aggregation kinetics of the *mAβ21* peptide at pH 12. The sigmoidal curve indicates amyloid formation reaching saturation after ~60 hours. Fluorescence values are normalized to the maximum intensity (a.u.). Data points represent the average of three independent scans, with error bars indicating the standard deviation.

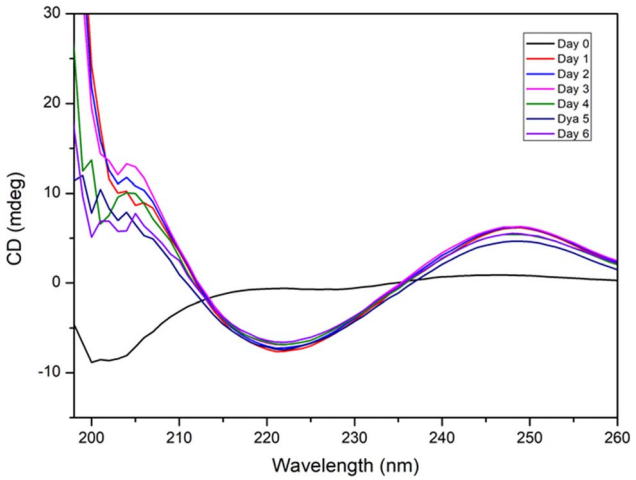

Fig. 4 Time-resolved circular dichroism (CD) spectra of the *mAβ21* peptide from Day 0 to Day 6, showing far-UV CD signals. The Day 0 spectrum reflects the predominantly disordered state of the freshly dissolved peptide, while the subsequent spectra reveal the progressive development of the β-sheet-rich secondary structure during the self-assembly process.

the maximum fibrillation process occurs at around 60 h and confirms the amyloid-forming nature of *mAβ21* under this pH 12 condition.

3.2.2 Circular dichroism spectroscopy. Circular dichroism (CD) spectroscopy is a powerful technique used widely to study the secondary structure characteristics and folding properties of proteins and peptides. It also gives a fair idea of the mutation effects, stability, *etc.*, in the protein/peptide of study.[22] The motivation for recording the far-UV CD spectra of all the peptides at different time points overlapping with the ThT fluorescence was to monitor the secondary structure of the self-assembling peptides that would further reiterate the structural characteristics of the same. The secondary structure information for the self-assembled peptides gives an insight into the structural composition of the designed peptide sequence attained during the amyloid formation. Fig. 4 illustrates the far-UV CD spectra of the designed *mAβ21* peptide in a pH 12 medium recorded at different time periods. The Day 0 spectrum shows minimal secondary structure features, while subsequent time points display a characteristic maximum at 250 nm, minima at about 220 nm (negative band near 220 nm), and maxima near 200 nm (positive band near 200 nm), features indicative of a β-sheet driven assembly. The secondary structure content of the *mAβ21* peptide was estimated using BeStSel deconvolution of the far-UV CD spectrum recorded on Day 1–6 (Table 1).[23]

The secondary structure elements present at the end of 6 days were calculated for the *mAβ21*, which exhibits about 0.6% α-helix content, 42.5% anti-parallel β-sheet content, 15.6% turn, and 41.3% disordered structures (Table 1 and Fig. S4(B)). The BeStSel fit showed a good agreement with experimental data, with a normalized root mean square deviation (NRMSD) of 0.08091 (Fig. S4(A)).

3.3 Morphological characterization of Aβ 1–42 based designed *mAβ21* peptide

3.3.1 Scanning electron microscopy (SEM) of the *mAβ21* peptide of amyloids. The morphological characterization of the self-assembled amyloid-like fibrils from the designed peptide sequence gives us essential information on the type of material the peptide has self-assembled into and the various intermediate stages in the fibrillization process. Scanning Electron Microscopy (SEM) is a powerful technique for viewing images of materials in the nano and micro scales. It gives us insight into various aspects of the peptide material, such as size and morphological characteristics. The designed self-assembled peptide was characterized by FE-SEM at different time points during the incubation and amyloid structure formation to trace the formation and growth of the peptide into stable structures. Fig. 5 depicts the morphology of the self-assembled peptide *mAβ21* formed at the beginning and at the end of 7 days post incubation in a pH 12 medium. To understand the different morphological evaluations during the aging or incubation period the amyloid nanostructure formation process of the *mAβ21* peptide was studied initially on Day 1, and the *mAβ21* peptide showcased an amorphous sponge-like morphology (Fig. 5(A)–(C)). These aggregates then slowly formed protofibrillar structures on Day 3 and Day 5 (Fig. S5). Interestingly, Day 7 SEM micrographs showed the formation of beautiful fractal pattern peptide-amyloid nanostructure morphologies resembling pine-tree branches (Fig. 5(D)–(F)). Upon measurement of the distances of the structures in the FE-SEM images, it was calculated that the length of the peptide ranged from 20–100 μm in *mAβ21* with an optimum length of around 70 μm (Fig. 5(G)).

3.3.2 Atomic force microscopy of *mAβ21* peptide amyloids. The information obtained from the Atomic Force Microscopy (AFM) images also sheds light on the morphology and size profiles of the assembled peptide. AFM is one of the powerful techniques to monitor the structures or morphologies of nano- or microstructures. Fig. 6(A) shows the AFM image of the *mAβ21*

Table 1 Secondary structure elements present in *mAβ21* peptide from Day 1–6 post-dissolution calculated from BeStSel analysis of the CD spectra

Secondary structure elements	Day 1	Day 2	Day 3	Day 4	Day 5	Day 6
α-Helix	1.7%	1.6%	1.5%	1.2%	1.1%	0.6%
β-Sheet (anti-parallel)	40.3%	41.0%	41.7%	41.7%	41.9%	42.5%
Turn	14.3%	15.2%	15.5%	15.6%	15.6%	15.6%
Others	43.6%	42.2%	41.3%	41.5%	41.4%	41.3%

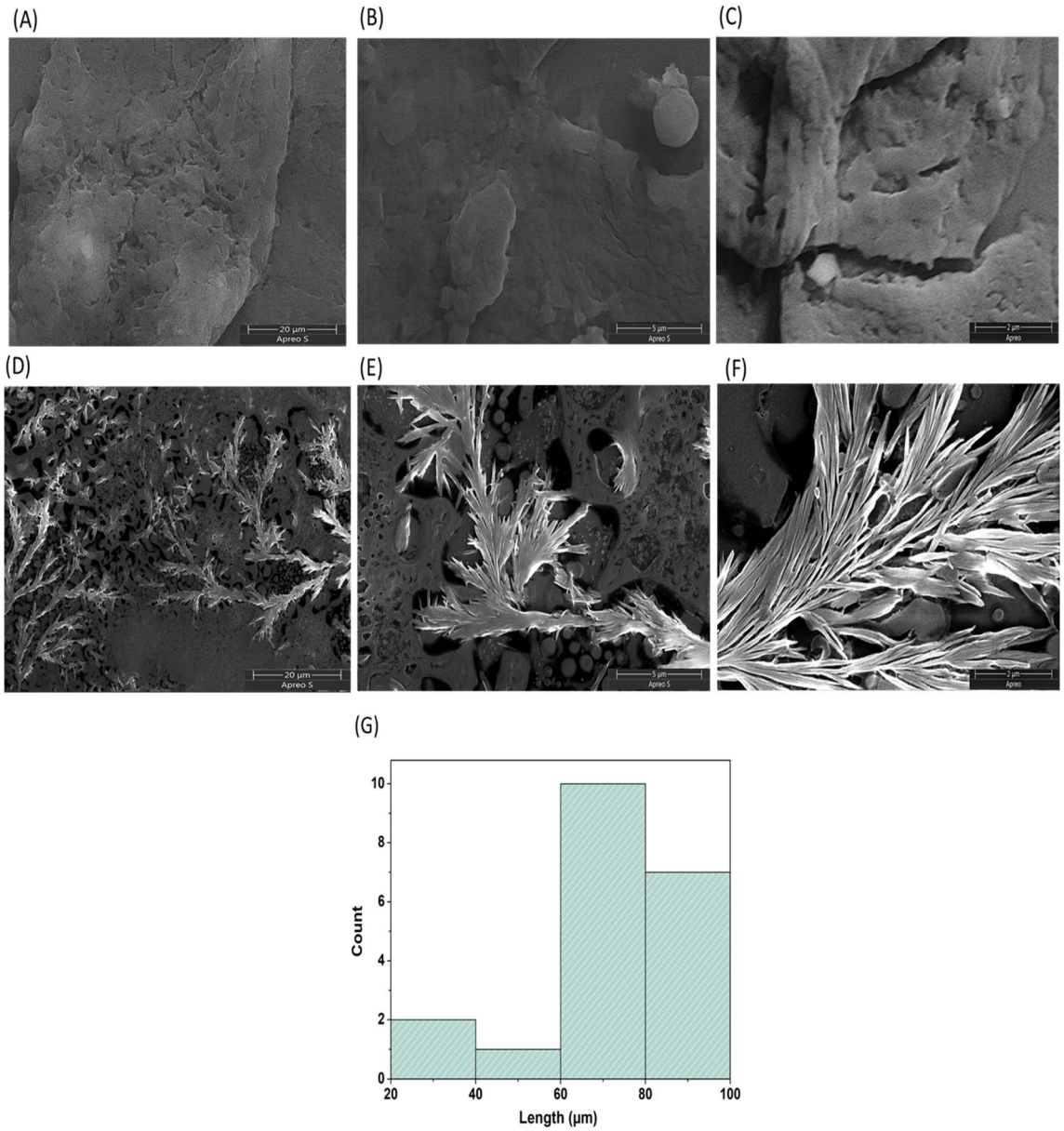

Fig. 5 Field emission scanning electron microscopy (FE-SEM) images of the *mAβ21* peptide at 1 day post incubation (A)–(C) and after 7 days of incubation (D)–(F) at pH 12. The self-assembled peptide structures exhibit pine-branch-like amyloid fibril morphology. The samples were thoroughly washed with ultrapure water to remove buffer salts prior to imaging. Both images are shown at the same magnification (scale bar = 20 μm, 5 μm, 2 μm). (G) Histogram showing the size distribution of the peptide fibril lengths based on SEM image analysis at Day 7.

peptide, 5 μL of 2.1×10^{-4} M, solution at pH 12 incubated for 7 days, drop cast and air dried on a glass cover slip. The AFM images of the amyloid structure of this peptide also show similar fractal-type nanostructure morphologies corroborating the SEM images of this peptide amyloid observed at an identical time frame of amyloid fibrillation growth. The width of the fibrils formed could be calculated from the atomic force microscope images ranging from 0.5–4 μm. For these *mAβ21* peptide-amyloids, the fibrillar structure size distribution is in the 0.7 μm to 1.2 μm range with 0.7 μm size material structure contributing to 25% of the overall size distribution. The size contribution decreasing with respect to the increasing width of the amyloid nanostructures (Fig. 6(B)). While AFM measurements revealed nanometer-scale fibril heights, SEM-derived lateral dimensions were larger, likely due to drying-induced flattening and sputter coating. These differences are consistent with known methodological biases.

3.3.3 Confocal microscopy of *mAβ21* peptide amyloids. Having studied the morphology of the self-assembled peptides through SEM and AFM, confocal microscope imaging was explored to detect these structures as this *mAβ21* peptide-amyloid is intrinsically fluorescent in nature. Hence no additional fluorescent dye such as ThT is required to be used in this experiment, and the observed signal was obtained from the

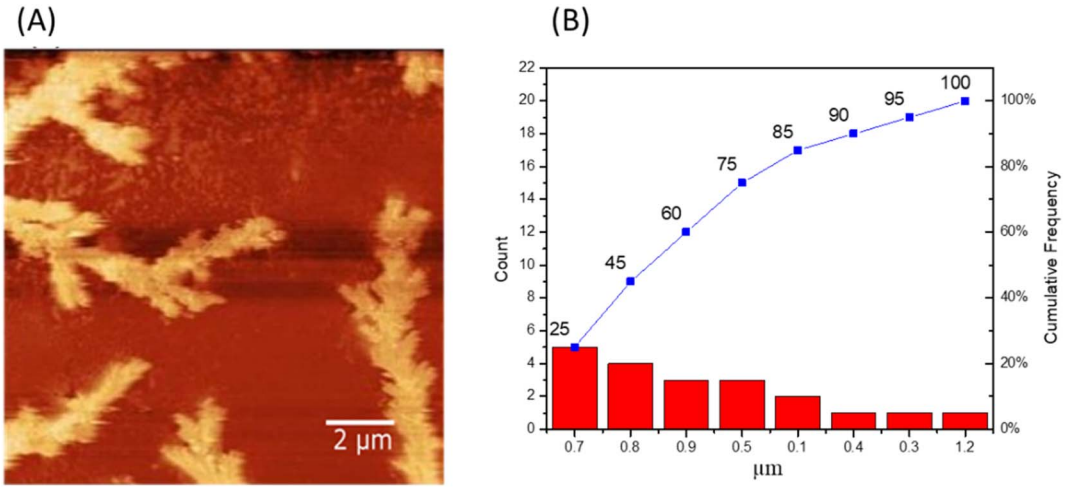

Fig. 6 (A) Atomic force microscopy (AFM) image of self-assembled *mAβ21* peptide fibrils on Day 7, showing branched amyloid-like morphology. (B) Corresponding fibril height distribution derived from AFM profiles, indicating the nanometer-scale thickness of individual fibrils. AFM provides nanometer-resolution height data, whereas SEM can present broadened lateral dimensions due to drying and coating effects.

sample directly under label-free imaging conditions. The *mAβ21* peptide-amyloid, 5 μL of 2.1×10^{-4} M, formed over 7 days incubation, drop cast on a glass slide covered with a glass cover slip was used for a confocal imaging study in the inverted glass slide mode. The direct and label-free excitation of the amyloid fibrils formed from the designed peptides exhibited blue-green fluorescence (470–510 nm) when excited using a 405 nm laser, as depicted in Fig. 7(B). This emission correlates with the peak observed in the solution-state fluorescence spectrum, suggesting that the blue-green signal arises from the peptide assemblies themselves. Fluorescence spectral analysis of the stock peptide solution with concentration 2.1×10^{-4} M, shown in (Fig. 7(C)), also indicated an emission at 450 nm;[24] the reason for this intrinsic fluorescence mechanism is plausibly the electronic transition induced by the direct excitation of the fibrils. Intrinsic fluorescence in amyloid fibrils has been attributed to electron delocalization through hydrogen bonds in cross-β sheet structures. Shukla *et al.*[25] first observed this in protein aggregates and proposed a mechanism involving low-energy transitions *via* backbone hydrogen bonding.[26] Del Mercato *et al.*[27] and Sharpe *et al.*[28] further demonstrated similar blue-range fluorescence in fibrillar peptides lacking aromatic residues. These emissions were Stokes-shifted, supporting

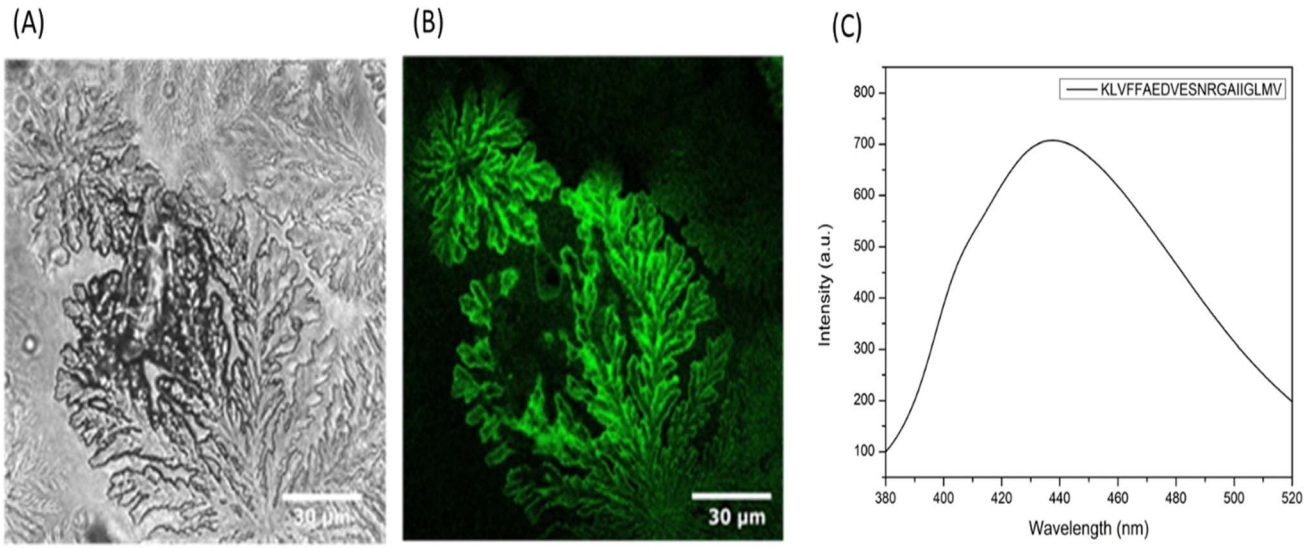

Fig. 7 (A) Bright-field and (B) confocal fluorescence images of self-assembled *mAβ21* peptide structures after 7 days of incubation at pH 12. Label-free excitation using a 405 nm laser source reveals blue-green fluorescence associated with the branched, amyloid-like morphology, consistent with intrinsic emission from peptide aggregates. (C) Fluorescence emission spectrum of the *mAβ21* peptide (2.1×10^{-4} M) in aqueous solution, recorded with an excitation wavelength of 355 nm. The emission maximum is observed near 445 nm, indicative of intrinsic fluorescence arising from the aggregated peptide structure.

intrinsic fluorescence as a general feature of amyloid-like assemblies.

The bright field and confocal images of the *mAβ21* peptide-amyloid are shown in Fig. 7(A) and (B), respectively. The morphological features obtained through confocal image study also show the amyloid-forming nature of this KLVFF-based peptide with the fractal morphology type as observed in SEM and AFM studies. The morphological analysis of *mAβ21* suggests that it forms fractal patterns resulting from diffusion-limited aggregation (DLA).[29] These patterns are comparatively different from KLVFF alone,[30] which forms fibrillar assembly.

3.3.4 Dynamic light scattering and zeta potential study of *mAβ21* peptide amyloids. The self-assembly of *mAβ21* was investigated using Dynamic Light Scattering (DLS), which estimates the average hydrodynamic radius of particles in solution. DLS measurements were performed at different time points to assess the progression of assembly in a pH 12 aqueous medium. The *mAβ21* peptide, initially after 1 hour of dissolution, exhibited sizes ranging from 41.6 nm, 50.2 and 78.5 nm diameter. The hydrodynamic size (*Z*-average) increased over time, reaching values of 986.3 nm, 1035 nm, and 1040 nm after 6 days of incubation (Fig. 8). As the concentration used for DLS study was relatively higher (100 μM peptide) in comparison to that in the ThT fluorescence enhancement study, the aggregation kinetics was relatively faster leading to faster amyloid maturation on the first day itself. Furthermore, the polydispersity index (PdI) remained high (0.481), consistent with the non-uniform population of branching assemblies.

3.3.5 Potentiometry pH titration and zeta potential measurement of the *mAβ21* peptide. The pH potentiometric titration was performed to broadly characterize the acid–base behavior of the *mAβ21* peptide across a wide pH range. While aggregation experiments were conducted at pH 12, this titration provides insight into the peptide's overall protonation profile and electrostatic environment, which may be relevant for interactions under variable pH conditions, such as in metal-binding studies. From the titration curve (Fig. S6), approximate values of $pK_1 = 2.9$, $pK_2 = 6.2$, and $pK_3 = 9.3$ were inferred, with the isoelectric point (pI) estimated as $(pK_1 + pK_2)/2 \approx 4.5$. These values are broadly consistent with the known side-chain pKa values of acidic (Asp, Glu: 3.65, 4.25) and basic (Lys, Arg: 10.53, 12.48) residues in the peptide.

Zeta potential measurements were performed for the *mAβ21* peptide across pH 2 to 12 to characterize the pH-dependent changes in net surface charge. The peptide exhibited positive charge at acidic pH, transitioned to near-neutral at pH 4, and became increasingly negative above pH 5 due to deprotonation of glutamic acid, aspartic acid, and lysine residues. At pH 12, relevant to the aggregation experiments, the peptide carried a net charge of −3.5 mV (Fig. S7). While not directly linked to aggregation behavior, these measurements provide insight into protonation states and electrostatic properties relevant for interpreting metal-binding potential and environmental responsiveness.

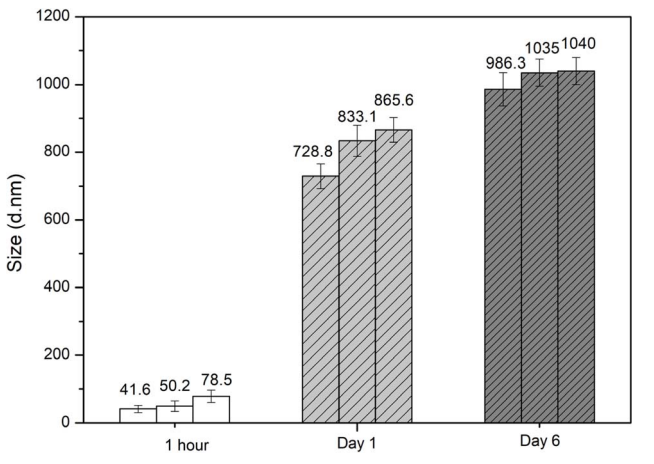

Fig. 8 Dynamic Light Scattering (DLS) analysis showing the average hydrodynamic diameter (*d* nm) of *mAβ21* peptide assemblies at pH 12, measured 1 hour post-dissolution and after incubation on Day 1 and Day 6. The increase in *Z*-average size over time suggests progressive aggregation.

3.4 Toxic metal lead (Pb) and uranium (U) binding properties of *mAβ21* peptide amyloids

Toxic metals lead and uranium were studied for their binding to the Aβ 1–42 based designed peptide, *mAβ21* self-assembled amyloid-peptide. Toxic metals, such as cadmium, mercury, *etc.*, have been known to increase amyloid-β structure formation upon exposure.[31,32] Metal-ion binding to amyloid β peptide generally showcases residue specificity that influences the structure and aggregation of the Aβ peptide. In the case of copper, zinc, and iron, metal ions predominantly bind to the histidine residues within the Aβ peptide, wherein the nitrogen present in the imidazole side-chains acts as the ligand for coordination along with oxygens of the other amino acid residues. To understand the metal-binding and sequestration capability of the *mAβ21* self-assembled amyloid-peptide we studied a mixture of metal ion solution containing 5 ppm each of mercury (Hg^{2+}), lead (Pb^{2+}), calcium (Ca^{2+}), chromium (Cr^{3+}), cobalt (Co^{2+}) nickel (Ni^{2+}), zinc (Zn^{2+}), and copper (Cu^{2+}). The metal ion binding preference of the *mAβ21* self-assembled amyloid-peptide was observed to be $Pb^{2+} > Hg^{2+} > Co^{2+} > Cr^{3+} > Cu^{2+} > Zn^{2+} > Ni^{2+} > Ca^{2+}$, (Fig. S8 and Table S2). We specifically investigated the binding of toxic metals such as lead (Pb) and uranium (U) to the *mAβ21* self-assembled amyloid-peptide in detail using spectroscopic techniques.

3.4.1 Lead metal ion binding of *mAβ21* peptide amyloids. The toxic metal lead has been known to bind to enzymes and regulatory proteins and coordinate with zinc finger proteins, having implications in physiological processes such as the development of neurological disorders. Lead is known to bind to nitrogen, oxygen, and sulfur atoms and is predominantly observed to be coordinated to glutamate and aspartate side-chains, apart from side-chain nitrogen, water molecules, and sulfur. Pb ions are especially prone to interact with Aβ and affect its aggregation.[33] They are also known to compete with essential metal ions such as zinc and calcium, increasing the expression of amyloid β peptide and modulating their aggregation.[32] Lead

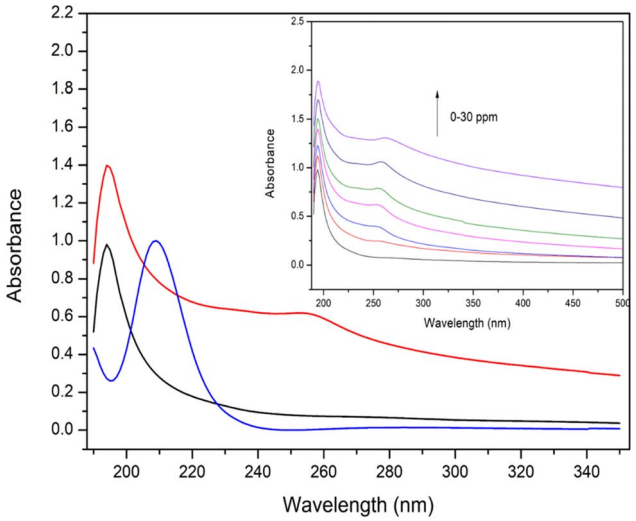

Fig. 9 UV absorption spectra for 50 μM of *mAβ21* peptide (black), 15 ppm of lead acetate (blue), and 50 μM *mAβ21*–lead acetate complex (15 ppm) (red). The inset shows the titration of the *mAβ21* peptide with increasing concentration of lead acetate (0–30 ppm).

ions (Pb^{2+}) are known to interact potentially with various residues present in the Aβ peptide, such as histidine and aspartate residues. However, the exact binding sites and coordination geometry of lead with Aβ are still being investigated. Given its affinity for nitrogen, oxygen, and sulfur-containing ligands, it is hypothesized that lead may coordinate with histidine, aspartic acid, glutamic acid, and/or cysteine residues similar to other metals like copper and zinc.

3.4.1.1 UV absorption spectroscopy for lead binding to mAβ21 peptide amyloids. The UV absorption peak of lead(II) acetate appears at 210 nm (Fig. 9), consistent with the detection of a signal for Pb^{2+} between 205 and 215 nm in the literature.[34] In the absence of lead, the peptide amyloid solution exhibits an absorbance peak at ~200 nm (Fig. 9), corresponding to π– π* transitions from the peptide backbone.[35] In the presence of peptide and lead acetate, the spectra reveal a shoulder at ~260 nm (Fig. 9), which is attributable to the ligand-to-metal charge transfer (LMCT) transition bands upon formation of the Pb(II)–peptide complexes. The new band at ~260 nm in the amyloid peptide + lead acetate spectra suggests lead-amyloid interactions, likely due to charge attraction and peptide ligand coordination with the metal ion.[36] This is consistent, for instance, with the appearance of a shoulder at around 240 nm for lysozyme–lead metal ion interaction.[37] The presence of more than one shoulder/peak is observed for the [Pb(*mAβ21* peptide)] lead–peptide complex at around 240 nm and 260 nm.

3.4.1.2 Atomic absorption spectroscopy for quantitative analysis of lead content and binding to self-assembled mAβ21 peptide amyloids. Self-assembled *mAβ21* peptide was incubated with increasing concentrations of lead acetate solution and filtered through a 5 kDa molecular weight cut-off filter. The concentration of the solution of lead acetate was monitored after filtration through atomic absorption spectroscopy. The 10 μM *mAβ21* self-assembled peptide amyloid material showed 15–30% binding and removal of lead ions from the solution at different lead acetate ppm levels (5, 10, 15, and 20 ppm), as shown in Fig. 10(A). The peptide : metal ratio at 10 μM peptide and 15 μM (5 ppm) of lead acetate corresponds to a 1 : 1.5 ratio, followed by 1 : 3 for 10 μM peptide and 30 μM (10 ppm) of lead acetate, 1 : 4.5 for 10 μM peptide and 45 μM (15 ppm) of lead acetate, and a 1 : 6 ratio for 10 μM peptide and 60 μM (20 ppm) of lead acetate (Fig. 10(A) and Table 2). Correspondingly while

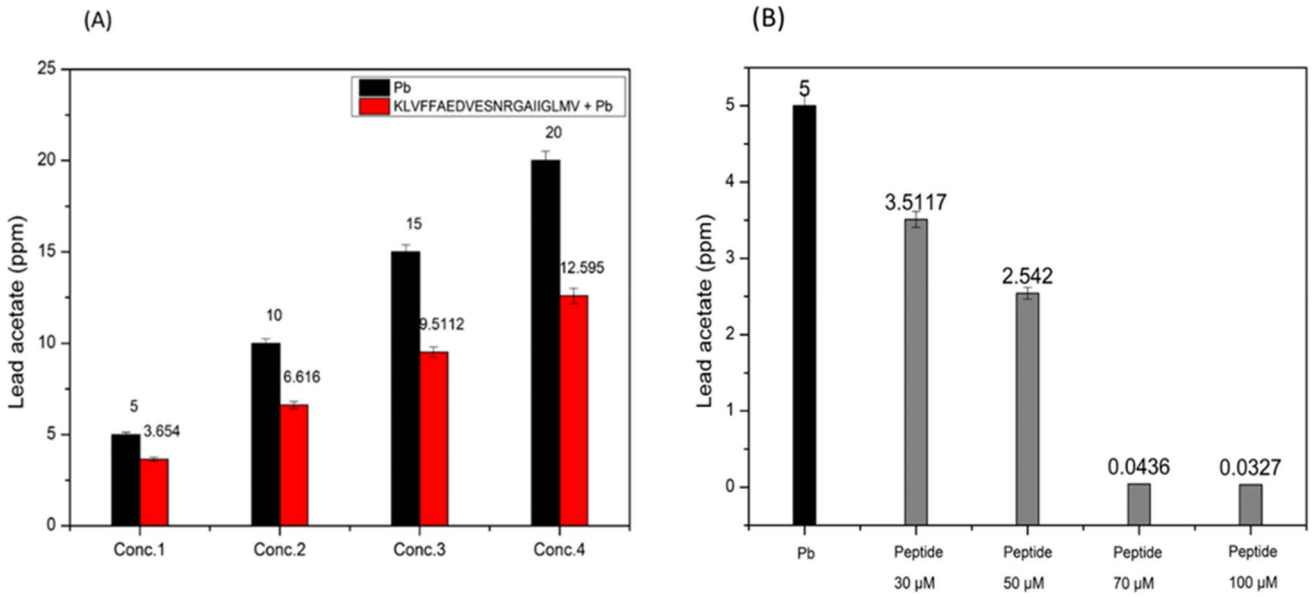

Fig. 10 Concentrations of lead acetate before and after filtration through the self-assembled peptide amyloid material *mAβ21*. (A) Increasing concentrations of lead acetate, 5 (15 μM), 10 (30 μM), 15 (45 μM), and 20 (60 μM) incubated with 10 μM of the *mAβ21* self-assembled peptide amyloid material and filtered through a 5 kDa cut-off filter. (B) Increasing concentration of the self-assembled peptide amyloid material *mAβ21* from 30, to 50, 70, and 100 μM incubated with 5 ppm lead acetate solution and filtered through a 5 kDa cut-off membrane filter.

Table 2 Lead (ppm) content in solution before and after incubation with *mAβ21* peptide amyloids

Peptide (μM)	Lead (before) (ppm)	Lead (after) (ppm)	%Pb removal
10	5 (15 μM)	3.6 (10.8 μM)	28%
10	10 (30 μM)	6.6 (19.2 μM)	34%
10	15 (45 μM)	9.5 (29.1 μM)	36.6%
10	20 (60 μM)	12.5 (40.5 μM)	37.5%

the concentration of the lead-acetate solution was kept constant (5 ppm or 15 μM) and the concentrations of the self-assembled *mAβ21* peptide are increased from 10 μM to 30, 50, 70, and 100 μM, resulting in peptide : metal ratios of 1 : 0.5 (30 μM), 1 : 0.3 (50 μM), 1 : 0.2 (75 μM), and 1 : 0.15 (100 μM), it was observed that there was a significant decrease in lead metal ion content upon increasing the concentration of the peptide to ~7.5 times the lead metal ion content, at 5 ppm (15 μM). Around ~30% decrease in lead content upon incubation with 10 μM of peptide amyloids, ~50% decrease in lead content for 30 μM of peptide amyloids, ~80% decrease of lead content for 70 μM peptide amyloids were observed, and more than 95% lead content was observed to be decreased for 100 μM concentration of the self-assembled peptide (Fig. 10(B)).

3.4.1.3 X-ray photoelectron spectroscopy for binding analysis of lead to self-assembled mAβ21 peptide amyloids. The X-ray photoelectron spectroscopy (XPS) study was employed for the analysis of the ability of the *mAβ21* peptide amyloid nanostructure to interact with Pb^{2+} and to further validate the decrease in lead acetate concentration observed from atomic absorption spectroscopy, by monitoring the Pb based binding energy peaks for lead acetate solution mixed and incubated with the self-assembled *mAβ21* peptide amyloids formed at pH 12. The XPS survey scan revealed the presence of carbon (C), nitrogen (N), and oxygen (O) atoms in the *mAβ21* self-assembled peptide amyloid material, while the XPS survey scan of only lead acetate showed the presence of Pb, C, and O, and the peptide–lead complexes were identified by the existence of binding energy (eV) associated with lead (Pb) features, in addition to carbon (C), nitrogen (N), and oxygen (O), as illustrated in Fig. 11(A). The X-ray photoelectron spectroscopy (XPS) spectra of lead compounds are characterized by two well-resolved peaks within the Pb 4f region (Fig. 11(B)), with a spin–orbit component Δ_{metal} of 4.87 eV (Table 3). The peak with higher binding energy at approximately 142 eV is attributed to Pb $4f_{5/2}$, while the lower energy peak at around 138 eV is assigned to Pb $4f_{7/2}$ (Table 3).[38] However, it should be noted that the binding energy values could be slightly influenced by the groups binding to the metal ion and the oxidation state of the lead metal ion.

Table 3 Binding energy (eV) values for lead acetate and the amyloid–lead complex

Sample	Binding energy (eV)	Δ_{metal} (eV)
Lead acetate	137.76 (Pb $4f_{7/2}$), 142.63 (Pb $4f_{5/2}$)	4.87
Peptide + lead acetate	137.62 (Pb $4f_{7/2}$), 142.49 (Pb $4f_{5/2}$)	4.87

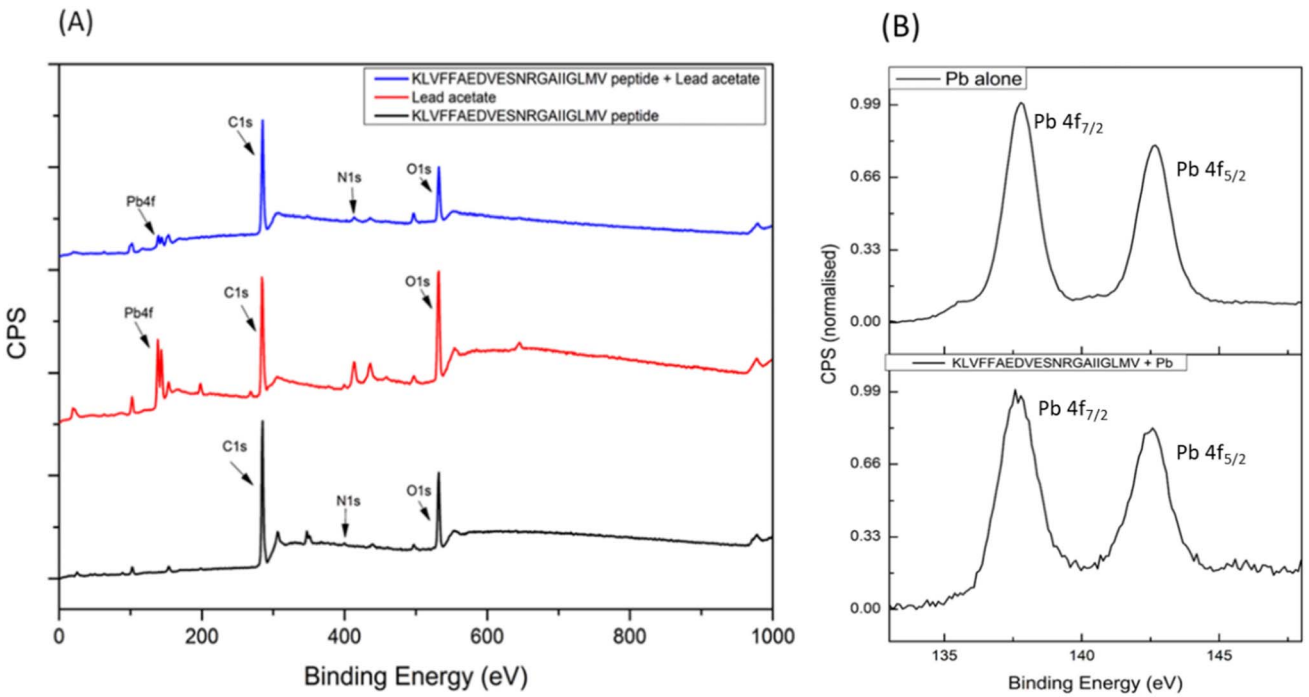

Fig. 11 (A) Survey scan of the *mAβ21* peptide, lead acetate, and the *mAβ21*–lead acetate complex. (B) Pb 4f narrow band scan XPS spectra of lead acetate alone (top panel) and 15 ppm lead acetate solution incubated with 50 μM of the *mAβ21* self-assembled peptide (bottom panel).

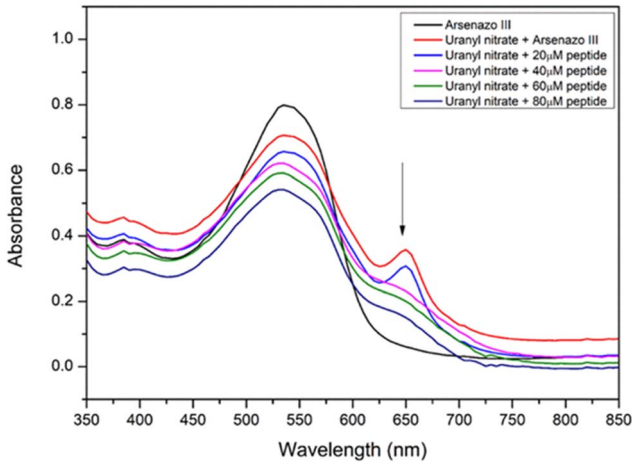

Fig. 12 UV-visible absorption spectra of arsenazo III dye in water (black), 12.9 μM (1 : 1 complex) of the uranyl nitrate – arsenazo III dye complex (red), and the uranyl nitrate–arsenazo complex (5 ppm/12.9 μM) incubated with *mAβ21* peptide amyloid (pH 12.0) at different concentrations, 20 μM (light blue), 40 μM (magenta), 60 μM (green) and 80 μM (dark blue).

Two peaks at around 142.63 and 137.76 eV of Pb(II) ions arising from Pb $4f_{5/2}$ and $4f_{7/2}$, respectively, in lead acetate are slightly shifted to lower binding energies upon binding to the self-assembled *mAβ21* peptide, appearing at 142.49 and 137.62 eV respectively. The addition of the self-assembled *mAβ21* peptide causes a shift in the binding energy of lead acetate, indicating complex formation rather than just surface adsorption. The charge of the *mAβ21* peptide under pH 12 conditions is −2 due to the presence of two deprotonated glutamic acid (E), one deprotonated aspartic acid (D), and one protonated arginine (R) amino acid residues upon complex formation with the lead (Pb^{2+}) ion, which possibly produces a neutral complex system to alter the electron density at the lead metal ion site.

3.4.2 Uranium metal ion binding analysis of *mAβ21* peptide amyloids

3.4.2.1 UV-visible spectroscopy studies for binding analysis of uranyl nitrate to self-assembled mAβ21 peptide amyloids. UV-visible absorption spectroscopy was employed to investigate the interaction between uranyl nitrate and the self-assembled *mAβ21* peptide amyloid material. Arsenazo III, a chromogenic dye forming 1 : 1 complexes with rare-earth metal ions, was used to detect uranium. Its characteristic absorption peak at 553 nm indicates the dye, while a band at 653 nm indicates complexation with uranyl(VI) nitrate.[39,40] This signal may shift or diminish depending on metal-dye stoichiometry. To assess the influence of peptide amyloid on this complex, varying concentrations of the peptide were incubated with the uranium

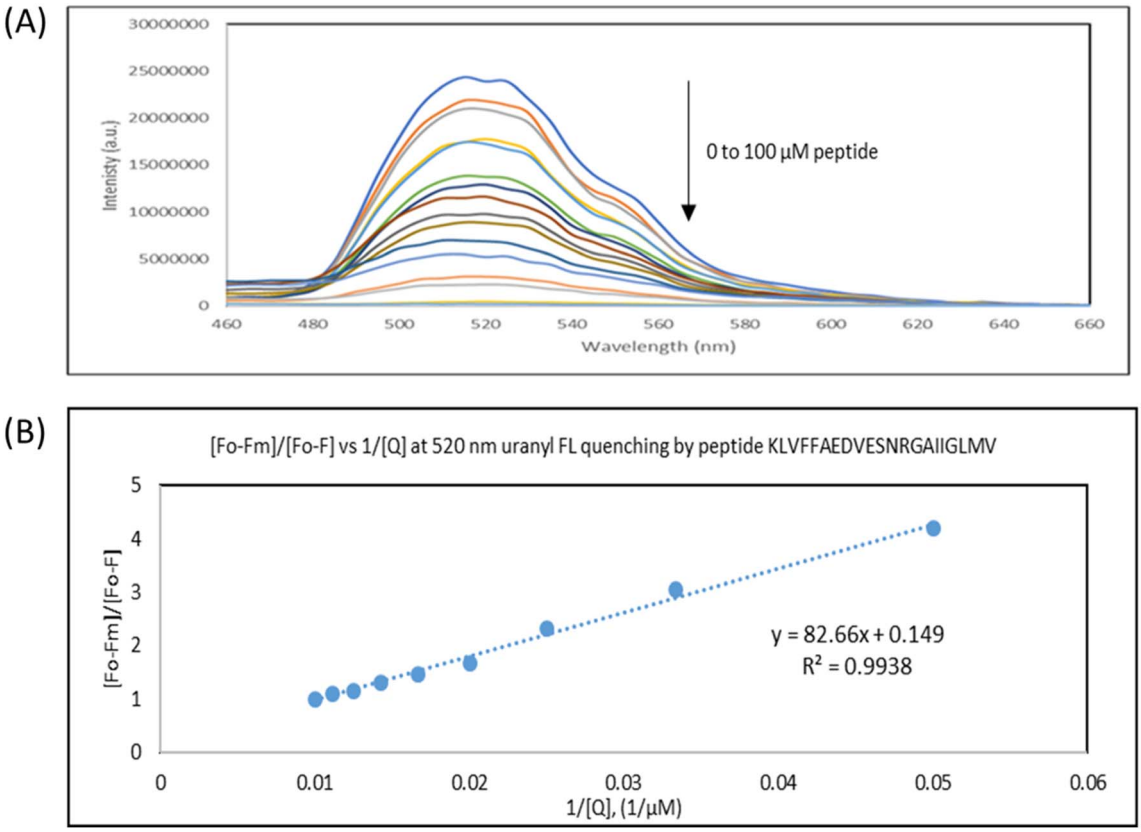

Fig. 13 Fluorescence emission quenching of uranyl nitrate by the *mAβ21* peptide. [A] Fluorescence emission quenching of 10 ppm uranyl nitrate solution titrated with increasing concentrations of the *mAβ21* self-assembled peptide (5, 10, 15, 20, 25, 30, 35, 40, 45, 50, 60, 70, 80, 90, and 100 μM). [B] Benesi–Hildebrand plot of $[(F_0 - F_m)/(F_0 - F)]$ (F_0 is the fluorescence intensity without the peptide and F_m is the minimum fluorescence intensity upon quenching), *vs.* [1/Q] (Q = peptide concentration in μM) showcasing 1 : 1 metal and peptide binding.

solution for 12 h. UV-vis analysis of the filtrate showed a concentration-dependent decrease in the 653 nm peak, indicating that uranium was retained by the peptide amyloid material, as shown in Fig. 12. This supports effective uranium binding by the self-assembled peptide.

3.4.2.2 Fluorescence spectroscopy studies for binding analysis of uranyl nitrate to self-assembled mAβ21 peptide amyloids. Fluorescence spectroscopy was used to confirm uranium binding to the self-assembled *mAβ21* peptide. Emission spectra were recorded for a 10 ppm uranyl nitrate solution titrated with increasing concentrations (5–100 μM) of peptide amyloid. A steady decrease in fluorescence intensity at 520 nm was observed with no significant shift in λ_{max}, indicating quenching upon binding. This result supports the uranium sequestration suggested by the UV-vis arsenazo-III assay. Stern–Volmer analysis was performed to evaluate the quenching mechanism (Fig. S9). The Stern–Volmer plot exhibited linearity at lower peptide concentrations, consistent with static quenching *via* ground-state complex formation between the uranyl ion and peptide amyloid. At higher concentrations, a deviation from linearity suggested the onset of dynamic quenching. The Stern–Volmer quenching constant (K_{SV}) was calculated to be 1.48×10^4 M^{-1}. The binding stoichiometry and association constant (K_A) were further determined using Benesi–Hildebrand plots assuming a 1 : 1 uranyl–peptide binding ratio (Fig. 13(B)). From the $[(F_0 - F_m)/(F_0 - F)]$ *vs.* $1/[Q]$ plot, an association constant K_A of 1.209×10^4 M^{-1} was obtained, confirming efficient uranyl binding by the peptide amyloid.

The designed Glu/Asp-rich regions are expected to chelate Pb^{2+} and UO_2^{2+} through carboxylate oxygens. In the metal–ligand binding Pb^{2+} may adopt hemi directed, asymmetric geometries, while UO_2^{2+} typically forms equatorial coordination with oxygen donor carboxylates.[41,42] Amyloid-forming peptides like Aβ are known to bind divalent metals (*e.g.*, Cu^{2+}, Zn^{2+}, and Pb^{2+}) *via* histidine and carboxylate residues;[43] poly histidine-rich peptides are also known to exhibit strong, selective metal binding.[44,45] Based on the functional groups present in the *mAβ21* peptide the following peptide amyloid–uranyl ion interaction mechanism is proposed. The uranyl–*mAβ21* peptide amyloid complex probably adopts an octahedral coordination environment involving one aspartic acid, two glutamic acid carboxylate groups and one oxygen from serine in the equatorial plane of the octahedral uranyl center, and further stability for uranyl binding is provided by the arginine side chain *via* an expected U═O···H–N hydrogen bonding interaction, as shown in Scheme 2.

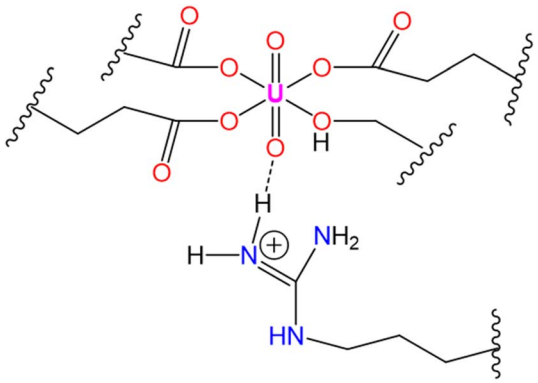

Scheme 2 Schematic representation of the coordination environment of uranyl–*mAβ21* peptide amyloid.

This study focused on the aggregated peptide material as the functional form for metal binding, leveraging its high surface area and ordered architecture. The studies performed for analysis of lead and uranium metal binding towards the *mAβ21* peptide have established its superior uranium and lead binding capabilities compared to our previously studied peptides EKKE and EKKEDRGDEKKE.[16] The %Pb removal for the *mAβ21* peptide is comparable to that of the EKKEDRGDEKKE peptide (34%) and much higher than that of the EKKE peptide alone (5%), while uranyl fluorescence quenching with *mAβ21* peptide amyloids show a better binding constant $K_A = 1.209 \times 10^4$ M^{-1}, than the EKKEDRGDEKKE ($K_A = 1.03 \times 10^4$ M^{-1}) and EKKE ($K_A = 0.16 \times 10^4$ M^{-1}) peptide amyloids.

4 Conclusions

The designed KLVFFAEDVESNRGAIIGLMV (*mAβ21*) peptide, which is the mutated version of KLVFFAEDVGSNKGAIIGLMV (16–36) residues of the amyloid β 1–42 peptide retained the ability to self-assemble into amyloid-like fibrils, even though two of its residues, G to E at position 25 and K to R at position 28 have been mutated. The formation of diffusion-limited aggregation (DLA) induced self-assembly of branched fibrils at alkaline pH also indicates the role of diphenylalanine, which has previously been reported to form such nanostructures. The self-assembled peptide also retains the β-sheet secondary structure content typically seen in amyloid fibrils and amyloid β 1–42 peptide. The *mAβ21* self-assembled peptide amyloid biomaterial also binds to lead and uranium metal ions. The metal ion binding process was observed from the decrease in lead metal content detected from atomic absorption spectroscopy, and the LMCT band was observed upon titration of increasing lead metal ions onto the self-assembling peptide-amyloid material. The fluorescence quenching of uranyl nitrate, along with the decrease in the absorption of the uranyl peak in the arsenazo III dye-based uranium estimation, proves the binding of uranium to the *mAβ21* peptide nanomaterial. The β-turn segment present in the original *mAβ21* Aβ 1–42 is hypothesized in this case to act as a metal-binding pocket, binding to both lead and uranium metal ions, due to the introduced E and R residues, respectively. The study of *mAβ21* is a comprehensive study on the nature of amyloid formation upon introducing point mutations to a known amyloid-forming peptide, along with assessing the ability of the self-assembled peptide amyloid to bind to toxic metals such as lead and uranium.

Author contributions

Aishwarya Natarajan: investigation, methodology, formal analysis, data curation, validation, writing – original draft, writing –

review and editing. Ramakrishna Vadrevu: conceptualization, funding acquisition, methodology, resources, supervision. Aruna Jyothi Kora: resources, supervision, writing – review and editing. Krishnan Rangan: conceptualization, funding acquisition, data curation, formal analysis, investigation, methodology, project administration, resources, supervision, writing – original draft, writing – review and editing.

Conflicts of interest

The authors affirm that they do not possess any identifiable personal or competing conflicts of interest that might have appeared to influence the research presented in this article.

Data availability

The data supporting this article have been included as part of the SI.

HPLC chromatogram, ESI(+)-mass spectrum, fluorescence emission spectra, BeStSel deconvolution output for the far-UV CD spectrum, FE-SEM images, potentiometric titration profile, zeta potential profile, percentage metal content of mixed metal ions after treatment with mAβ21 peptide amyloids and fluorescence emission quenching plot. See DOI: **https://doi.org/10.1039/d5na00228a**.

Abbreviations

K	Lysine
L	Leucine
V	Valine
F	Phenylalanine
A	Alanine
E	Glutamic acid
D	Aspartic acid
S	Serine
N	Asparagine
R	Arginine
G	Glycine
I	Isoleucine
M	Methionine
ThT	Thioflavin T
CD	Circular dichroism
HFIP	1,1,1,3,3,3-Hexafluoro-2-propanol
FE-SEM	Field Emission Scanning Electron Microscopy
AFM	Atomic Force Microscopy
UV	Ultra-Violet
XPS	X-ray Photoelectron Spectroscopy
CPS	Counts per second
eV	Electron volt

Acknowledgements

AN is grateful to the Board of Research in Nuclear Sciences (BRNS), Department of Atomic Energy (DAE, Government of India) for providing a research fellowship through the funded grant. The research is supported by a grant from BRNS, DAE, Govt. of India (37(1)14/11/2-17-BRNS/37013) to RV and KR. The authors gratefully acknowledge the Central Analytical Laboratory, Birla Institute of Technology and Science Pilani, Hyderabad Campus, for providing access to FE-SEM, and fluorescence, UV-visible, and X-ray photoelectron spectroscopy facilities. This manuscript is dedicated to Late Prof. Ramakrishna Vadrevu.

References

1 I. Cherny and E. Gazit, Amyloids: Not only pathological agents but also ordered nanomaterials, *Angew. Chem., Int. Ed.*, 2008, **47**, 4062–4069, DOI: **10.1002/anie.200703133**.
2 B. J. Kim, D. Yang and B. Xu, Emerging Applications of Supramolecular Peptide Assemblies, *Trends Chem.*, 2020, **2**(1), 71–83, DOI: **10.1016/j.trechm.2019.09.004**.
3 S. Mankar, A. Anoop, S. Sen and S. K. Maji, Nanomaterials: amyloids reflect their brighter side, *Nano Rev.*, 2011, **2**(1), 6032, DOI: **10.3402/nano.v2i0.6032**.
4 S. Bolisetty and R. Mezzenga, Amyloid-carbon hybrid membranes for universal water purification, *Nat. Nanotechnol.*, 2016, **11**(4), 365–371, DOI: **10.1038/nnano.2015.310**.
5 F. Yang, Q. Yang, M. Chen, C. Luo, W. Chen and P. Yang, Toxic metal ion sequestration by amyloid-mediated fast coacervation, *Cell Rep. Phys. Sci.*, 2021, **2**(3), 100379, DOI: **10.1016/j.xcrp.2021.100379**.
6 S. Pradhan, A. K. Brooks and V. K. Yadavalli, Nature-derived materials for the fabrication of functional biodevices, *Mater. Today Bio*, 2020, **7**, 100065, DOI: **10.1016/j.mtbio.2020.100065**.
7 S. Liu, *et al.*, Biomimetic natural biomaterials for tissue engineering and regenerative medicine: new biosynthesis methods, recent advances, and emerging applications, *Mil. Med. Res.*, 2023, **10**(1), 16, DOI: **10.1186/s40779-023-00448-w**.
8 E. Troy, M. A. Tilbury, A. M. Power and J. G. Wall, Nature-Based Biomaterials and Their Application in Biomedicine, *Polymers*, 2021, **13**(19), 3321, DOI: **10.3390/polym13193321**.
9 M. Kumar, A. Seth, A. K. Singh, M. S. Rajput and M. Sikandar, Remediation strategies for heavy metals contaminated ecosystem: A review, *Environ. Sustainability Indic.*, 2021, **12**, 100155, DOI: **10.1016/j.indic.2021.100155**.
10 C. Cheignon, M. Tomas, D. Bonnefont-Rousselot, P. Faller, C. Hureau and F. Collin, Oxidative stress and the amyloid beta peptide in Alzheimer's disease, *Redox Biol.*, 2018, **14**, 450–464, DOI: **10.1016/j.redox.2017.10.014**.
11 F. Hane, G. Tran, S. J. Attwood and Z. Leonenko, Cu(2+) affects amyloid-β (1-42) aggregation by increasing peptide-peptide binding forces, *PLoS One*, 2013, **8**(3), e59005, DOI: **10.1371/journal.pone.0059005**.
12 Schrödinger LLC, *The {PyMOL} Molecular Graphics System*, Version~1.8, 2015.
13 N. J. Anthis and G. M. Clore, Sequence-specific determination of protein and peptide concentrations by absorbance at 205 nm, *Protein Sci.*, 2013, **22**(6), 851–858, DOI: **10.1002/pro.2253**.

14 C. Xue, T. Y. Lin, D. Chang and Z. Guo, Thioflavin T as an amyloid dye: Fibril quantification, optimal concentration and effect on aggregation, *R. Soc. Open Sci.*, 2017, **4**(1), 160696, DOI: 10.1098/rsos.160696.

15 M. Biancalana and S. Koide, Molecular mechanism of Thioflavin-T binding to amyloid fibrils, *Biochim. Biophys. Acta*, 2010, **1804**, 1405–1412, DOI: 10.1016/j.bbapap.2010.04.001.

16 A. Natarajan, L. R. Vadrevu and K. Rangan, DRGD-linked charged EKKE dimeric dodecapeptide: pH-based amyloid nanostructures and their application in lead and uranium binding, *RSC Adv.*, 2024, **14**(13), 9200–9217, DOI: 10.1039/d3ra08261j.

17 M. Wojdyr, Fityk: A general-purpose peak fitting program, *J. Appl. Crystallogr.*, 2010, **43**(5), 1126–1128, DOI: 10.1107/S0021889810030499.

18 J. R. Lakowicz, *Principles of fluorescence spectroscopy*, 2006, DOI: 10.1007/978-0-387-46312-4.

19 H. A. Benesi and J. H. Hildebrand, A Spectrophotometric Investigation of the Interaction of Iodine with Aromatic Hydrocarbons, *J. Am. Chem. Soc.*, 1949, **71**(8), 2703–2707, DOI: 10.1021/ja01176a030.

20 L. Zhou, *et al.*, A protein engineered to bind uranyl selectively and with femtomolar affinity, *Nat. Chem.*, 2014, **6**(3), 236–241, DOI: 10.1038/nchem.1856.

21 C. Bortolini, *et al.*, Rapid Growth of Acetylated Aβ(16-20) into Macroscopic Crystals, *ACS Nano*, 2018, **12**(6), 5408–5416, DOI: 10.1021/acsnano.8b00448.

22 N. J. Greenfield, Using circular dichroism spectra to estimate protein secondary structure, *Nat. Protoc.*, 2007, **1**(6), 2876–2890, DOI: 10.1038/nprot.2006.202.

23 A. Micsonai, *et al.*, BeStSel: A web server for accurate protein secondary structure prediction and fold recognition from the circular dichroism spectra, *Nucleic Acids Res.*, 2018, **46**(W1), W315–W322, DOI: 10.1093/nar/gky497.

24 A. Natarajan, K. Rangan and R. Vadrevu, Self-assembly of a peptide sequence, EKKE, composed of exclusively charged amino acids: Role of charge in morphology and lead binding, *J. Pept. Sci.*, 2022, **29**(2), e3451, DOI: 10.1002/psc.3451.

25 A. Shukla, S. Mukherjee, S. Sharma, V. Agrawal, K. V. R. Kishan and P. Guptasarma, A novel UV laser-induced visible blue radiation from protein crystals and aggregates: Scattering artifacts or fluorescence transitions of peptide electrons delocalized through hydrogen bonding?, *Arch. Biochem. Biophys.*, 2004, **428**, 144–153, DOI: 10.1016/j.abb.2004.05.007.

26 O. J. Rolinski, M. Amaro and D. J. S. Birch, Early detection of amyloid aggregation using intrinsic fluorescence, *Biosens. Bioelectron.*, 2010, **25**(10), 2249–2252, DOI: 10.1016/j.bios.2010.03.005.

27 L. L. Del Mercato, *et al.*, Charge transport and intrinsic fluorescence in amyloid-like fibrils, *Proc. Natl. Acad. Sci. U. S. A.*, 2007, **104**(46), 18019–18024, DOI: 10.1073/pnas.0702843104.

28 S. Sharpe, K. Simonetti, J. Yau and P. Walsh, Solid-state NMR characterization of autofluorescent fibrils formed by the elastin-derived peptide GVGVAGVG, *Biomacromolecules*, 2011, **12**, 1546–1555, DOI: 10.1021/bm101486s.

29 E. Mayans, *et al.*, Hierarchical self-assembly of di-, tri- and tetraphenylalanine peptides capped with two fluorenyl functionalities: From polymorphs to dendrites, *Soft Matter*, 2016, **12**(24), 5475–5488, DOI: 10.1039/c6sm00337k.

30 M. J. Krysmann, V. Castelletto, A. Kelarakis, I. W. Hamley, R. A. Hule and D. J. Pochan, Self-Assembly and Hydrogelation of an Amyloid Peptide Fragment, *Biochemistry*, 2008, **47**(16), 4597–4605, DOI: 10.1021/bi8000616.

31 T. J. Huat, J. Camats-Perna, E. A. Newcombe, N. Valmas, M. Kitazawa and R. Medeiros, Metal Toxicity Links to Alzheimer's Disease and Neuroinflammation, *J. Mol. Biol.*, 2019, **431**(9), 1843–1868, DOI: 10.1016/j.jmb.2019.01.018.

32 A. Ashok, N. K. Rai, S. Tripathi and S. Bandyopadhyay, Exposure to As-, Cd-, and Pb-Mixture Induces Aβ, Amyloidogenic APP Processing and Cognitive Impairments via Oxidative Stress-Dependent Neuroinflammation in Young Rats, *Toxicol. Sci.*, 2015, **143**(1), 64–80, DOI: 10.1093/toxsci/kfu208.

33 C. Wallin, *et al.*, Alzheimer's disease and cigarette smoke components: effects of nicotine, PAHs, and Cd(II), Cr(III), Pb(II), Pb(IV) ions on amyloid-β peptide aggregation, *Sci. Rep.*, 2017, **7**(1), 14423, DOI: 10.1038/s41598-017-13759-5.

34 C. H. Tan, Y. C. Moo, M. Z. Mat Jafri, and H. S. Lim, UV spectroscopy determination of aqueous lead and copper ions in water, in *Optical Sensing and Detection III*, 2014, DOI: 10.1117/12.2052349.

35 M. A. Saraiva, Interpretation of α-synuclein UV absorption spectra in the peptide bond and the aromatic regions, *J. Photochem. Photobiol., B*, 2020, **212**, 112022, DOI: 10.1016/j.jphotobiol.2020.112022.

36 V. Cangelosi, L. Ruckthong, and V. L. Pecoraro, Lead(II) binding in natural and artificial proteins, in *Lead: its Effects on Environment and Health*, 2017, vol. 17, pp. 271–317, DOI: 10.1515/9783110434330-010.

37 H. Zhang, F. Hao and R. Liu, Interactions of lead (II) acetate with the enzyme lysozyme: A spectroscopic investigation, *J. Lumin.*, 2013, **142**, 144–149, DOI: 10.1016/j.jlumin.2013.03.061.

38 S. Rondon and P. M. A. Sherwood, Core Level and Valence Band Spectra of Lead by XPS, *Surf. Sci. Spectra*, 1998, **5**(2), 83–89, DOI: 10.1116/1.1247864.

39 C. Hogendoorn, *et al.*, Facile Arsenazo III-based assay for monitoring rare earth element depletion from cultivation media for methanotrophic and methylotrophic bacteria, *Appl. Environ. Microbiol.*, 2018, **84**, e02887, DOI: 10.1128/AEM.02887-17.

40 M. H. Khan, P. Warwick and N. Evans, Spectrophotometric determination of uranium with arsenazo-III in perchloric acid, *Chemosphere*, 2006, **63**(7), 1165–1169, DOI: 10.1016/j.chemosphere.2005.09.060.

41 S. H. Seda, J. Janczak and J. Lisowski, Synthesis and structural characterisation of nickel 15-metallacrown-5

complexes with lanthanide (III) and lead (II) ions: Influence of the central metal ion size on the spin state of peripheral nickel (II) ions, *Inorg. Chem. Commun.*, 2006, **9**(8), 792–796, DOI: **10.1016/j.inoche.2006.04.026**.

42 T. Loiseau, I. Mihalcea, N. Henry and C. Volkringer, The crystal chemistry of uranium carboxylates, *Coord. Chem. Rev.*, 2014, **266**, 69–109, DOI: **10.1016/j.ccr.2013.08.038**.

43 M. Rana and A. K. Sharma, Cu and Zn interactions with Aβ peptides: consequence of coordination on aggregation and formation of neurotoxic soluble Aβ oligomers, *Metallomics*, 2019, **11**(1), 64–84, DOI: **10.1039/c8mt00203g**.

44 L. G. P. Nunes, T. Reichert and M. Teresa Machini, His-rich peptides, gly-and his-rich peptides: Functionally versatile compounds with potential multi-purpose applications, *Int. J. Pept. Res. Ther.*, 2021, 1–19, DOI: **10.1007/s10989-021-10302-z**.

45 Y.-B. Zeng, N. Yang and H. Sun, Metal-binding properties of an Hpn-like histidine-rich protein, *Chem.–Eur. J.*, 2011, **17**(21), 5852–5860, DOI: **10.1002/chem.201100279**.